

The synthesis of Bi_2Te_3 nanobelts by vapor–liquid–solid method and their electrical transport properties

Q. Wei · Y. Su · C. J. Yang · Z. G. Liu ·
H. N. Xu · Y. D. Xia · J. Yin

Received: 17 August 2010/Accepted: 9 November 2010/Published online: 2 December 2010
© Springer Science+Business Media, LLC 2010

Abstract Bi_2Te_3 nanobelts were synthesized on quartz substrates by gold-mediated vapor–liquid–solid (VLS) growth through a thermal evaporation process. The structure and morphology were characterized by using scanning electron microscopy (SEM) and transmission electron microscopy (TEM). The temperature dependence of the conductivity of Bi_2Te_3 single crystal nanobelt shows a semiconductor behavior, and the activation energy was calculated as about 25 meV, indicating that the thermal activation of carriers from the impurity level dominates the transport property.

Introduction

Bismuth telluride (Bi_2Te_3) is a narrow energy gap semiconductor material [1] with rhombohedral structure. This structure is mostly simply visualized in terms of a layer structure and a hexagonal unit cell [2]. Recently, Bismuth telluride has attracted much attention due to its topological insulator behavior as predicted by Zhang et al. [3]. Topological insulators are new states of quantum matter in which surface states residing in the bulk insulating gap of such systems are protected by time-reversal symmetry [4]. The study of such states was originally inspired by the robustness to scattering of conducting edge states in quantum Hall systems [5]. When electrons are subjected to

a large external magnetic field, the conventional charge quantum Hall effect [6, 7] dictates that an electronic excitation gap is generated in the bulk sample, but metallic conduction is permitted at the boundary. Recent theoretical models suggest that certain bulk insulators with large spin-orbit interactions may also naturally support conducting topological boundary states in the quantum limit [8]. Owing to this unique property, Bi_2Te_3 has potential application in developing next-generation quantum computing devices that may incorporate ‘light-like’ bulk carriers and spin-textured surface currents.

Besides, lots of interests are also focused on its thermoelectric properties [9–11]. Thermoelectric (TE) devices, directly converting thermal energy to electricity, could help to relieve the severe problems of energy shortage and environmental pollution to some extent. However, the efficiencies of the fabricated TE devices are not high enough for the practical application because of the relatively low thermoelectric figure of merit (ZT). According to the theoretical predictions, [12–15] TE performance will be enhanced with confined dimensions. Thus, the synthesis of one-dimensional nanobelts of Bismuth telluride is strongly desired not only for the improvement of TE performance but also for the understanding of transport mechanism within a confined nanoscale. Some works have been done to synthesize one-dimensional Bi_2Te_3 nanostructures, such as nanowires [16–18] and nanotubes [19, 20] through the electrodeposition process and hydrothermal method, whereas it is not very easy to obtain single crystal products through these processes. Polycrystalline nature of the products could play a negative effect on enhancing the TE performance due to the boundary scattering [17–19]. To our knowledge, there have been few reports on the synthesis of Bi_2Te_3 nanobelts. Here, we report a simple method for synthesizing single crystal Bi_2Te_3 nanobelts through

Q. Wei · Y. Su · C. J. Yang · Z. G. Liu (✉)

H. N. Xu · Y. D. Xia · J. Yin (✉)

National Laboratory of Solid State Microstructures and Department of Materials Science and Engineering, Nanjing University, Nanjing 210093, People’s Republic of China
e-mail: liuzg@nju.edu.cn

J. Yin

e-mail: jyin@nju.edu.cn

vapor–liquid–solid (VLS) process. The temperature dependence of the conductivity for Bi_2Te_3 single crystal nanobelts has also been investigated

Experimental

Bi_2Te_3 single crystal nanobelts were synthesized based on the VLS mechanism by using the thermal evaporation of Bi_2Te_3 particles in a sealed quartz tube with a vacuum of 4×10^{-1} pa. The quartz tube was 150 mm in length, and 15 mm in radius. The growth apparatus of Bi_2Te_3 nanobelts is schematically drawn in Fig. 1. Bi_2Te_3 particles were used as precursor materials which were prepared by using levitation melting method with a mixture of pure (99.99%) Bi and Te powder. A quartz substrate (10 mm × 30 mm) deposited with Au colloid as catalyst was placed in the low-temperature region in the quartz tube. The distance between Bi_2Te_3 particles and the substrate is about 50 mm. Then the quartz tube was placed in a tube furnace and the nanobelts were grown at 500°C for 300 min. The heating rate was controlled as 6°C/min.

The morphology of the as-synthesized Bi_2Te_3 nanobelts was analyzed by using scanning electron microscopy (SEM, Hitachi S-3400 N), and the structure of Bi_2Te_3 nanobelts was investigated by using transmission electron microscopy (TEM, JEOL JEM-200CX), energy dispersive spectroscopy (EDS) and high resolution transmission electron microscopy (HRTEM). The samples for TEM observation were prepared by sonicating quartz substrate covered with Bi_2Te_3 single crystal nanobelts in ethanol for 10 s to release the nanobelts from the substrate, and then dispersing the solution onto a holey carbon copper grid (300 mesh).

To measure the electric property, Bi_2Te_3 single crystal nanobelts were released from the substrate by ultrasonic agitation and suspended in ethanol. Then a drop of 0.05 ml solution containing Bi_2Te_3 single crystal nanobelts was deposited on a chip which contains arrays of underlying platinum (Pt) electrode bars separated 2 μm with each other. The chips were fabricated through the following process: first, a thermally oxidized Si substrate with a 200-nm SiO_2 layer was covered with photoresist and

patterned by using a standard photolithographic process with the assistance of predesigned mask. Next, the chip was covered with Ti (10 nm, as adhesion layer) and Pt (100 nm) by using magnetron sputtering technique, respectively. Last, a lift-off process was used to remove unwanted Ti and Pt. Then, Pt top electrodes were deposited on the cross area of the nanobelt and Pt bottom electrodes by using focused ion beam (FIB) technique to enhance the electrical contact. The Pt-hydrocarbon gas was used as precursor to deposit Pt electrode. The measurement of electrical property was carried out with a probe station (model Summit 12000M, Cascade Microtech) and a Keithley 4200 semiconductor characterization system. I – V curves were measured at various temperatures on the probe station using a thermal chuck system (Model ETC-200 L, ESPEC, Japan). All of the electrical measurements were taken in nitrogen atmosphere.

Results and discussions

Figure 2a shows a SEM image of the as-grown nanobelts. The average width of Bi_2Te_3 nanobelts is 200 nm and the average length is about 10 μm . The inset in Fig. 2a shows an enlarged SEM image containing three individual nanobelts. The belt-like morphology of products can be well recognized according this enlarged SEM image, where one nanobelt is highly curved with a thickness far smaller than the width. The product morphology and microstructures were carefully studied by using TEM, HRTEM, EDS, and selected area electron diffraction (SAED). Figure 2c shows a typical Bi_2Te_3 nanobelt with an Au tip on the end of the belt. The width of the Bi_2Te_3 nanobelt is 150 nm and the size of Au tip is 140 nm. Energy dispersive spectroscopy collected from the center (Fig. 2e) and the end of the belt (Fig. 2d) show that the center is composed of Bi and Te, and the end only contains Au (the C and Cu peaks come from the carbon copper grid). This indicates that Au particles act as the catalyst in the growing process of Bi_2Te_3 nanobelts. The control experiment of no Au catalysts was also conducted, and the SEM image of the products is shown in Fig. 2b. It was observed that there were only few

Fig. 1 Schematic diagram of the furnace applied in the nanobelt growth process

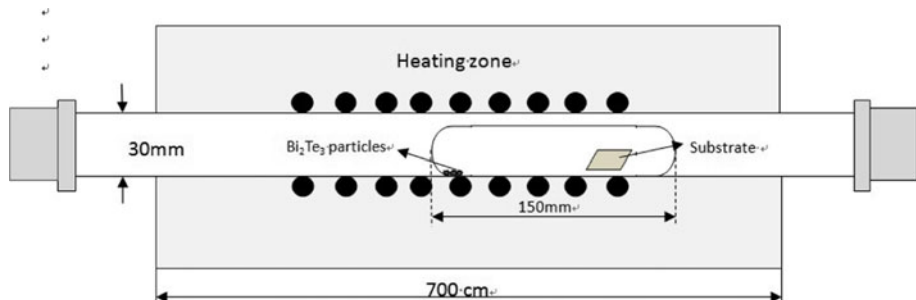
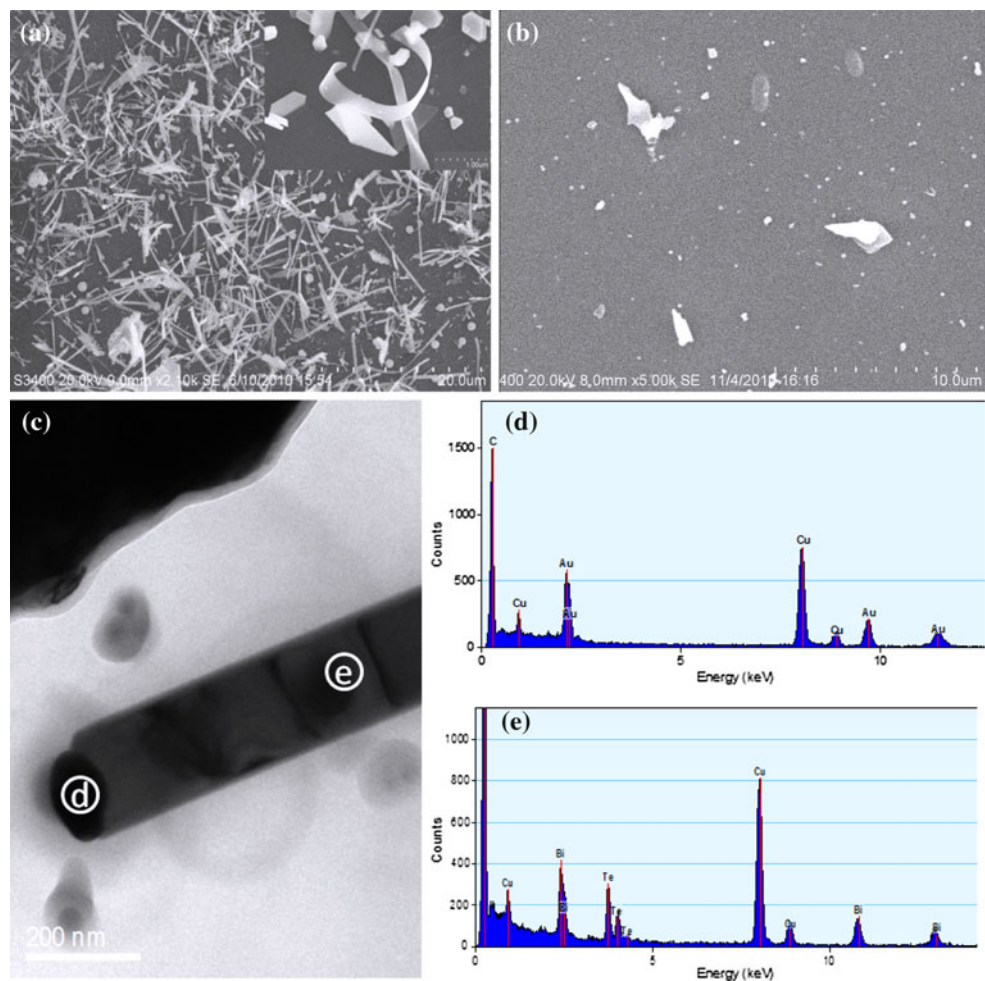


Fig. 2 **a** SEM image of Bi_2Te_3 nanobelts, inset: enlarged SEM image of Bi_2Te_3 nanobelts, including two wide nanobelts, **b** SEM image of a sample without Au catalysts, **c** TEM image of a single Bi_2Te_3 nanobelt with a Au tip on the end of the belt, **d** EDS collected from the end of the nanobelt, **e** EDS collected from the center of a Bi_2Te_3 nanobelt



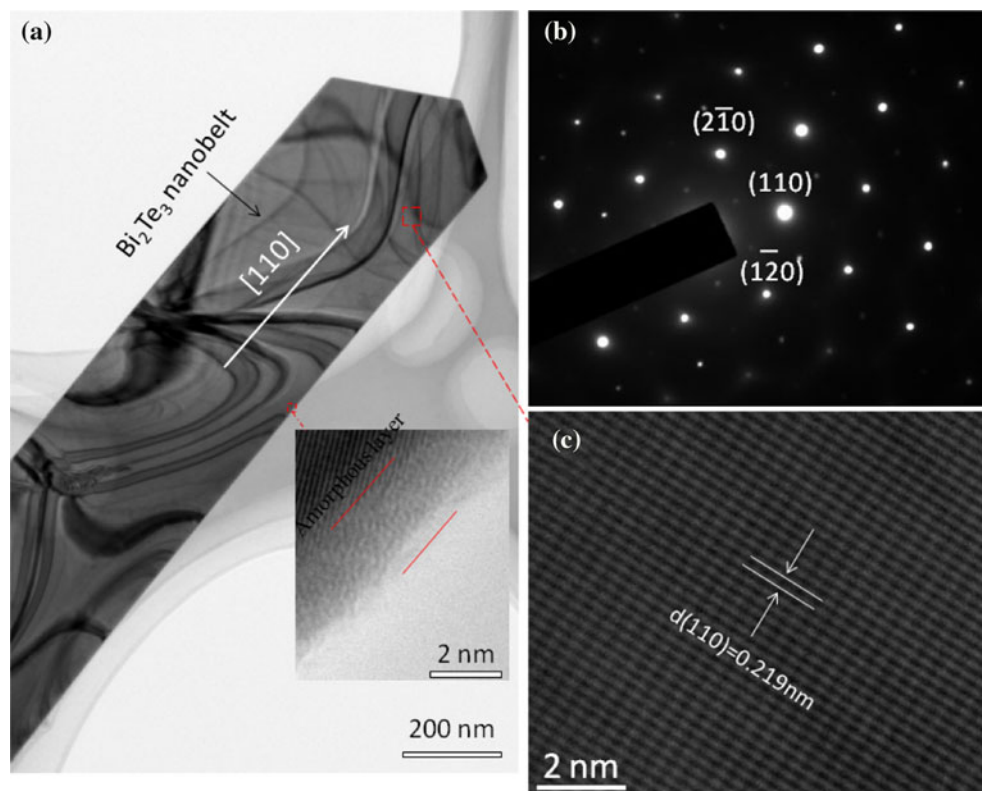
tiny Bi_2Te_3 particles and blocks, and no nanobelt on the quartz substrate appears. The results clearly demonstrate that the growth of Bi_2Te_3 nanobelts is based on the gold-mediated VLS process.

Figure 3a shows a typical low-magnification TEM image of an individual Bi_2Te_3 nanobelt with a width of 160 nm. The nanobelts were uniform in diameter and there is an amorphous layer of 2–3 nm on their surface, as shown by the inset in Fig. 3a. The formation of the amorphous layer can be attributed to the oxidization of Bi_2Te_3 nanobelts due to the fact that the vacuum in the sealed quartz tube is not high enough. Fig. 3b shows the selected-area diffraction pattern (SAED) of a single Bi_2Te_3 nanobelt. The SAED pattern was indexed to the hexagonal lattice of Bi_2Te_3 ($a = 4.385 \text{ \AA}$, $c = 30.483 \text{ \AA}$) with the electron beam direction along the [001] zone axis, indicating that the nanobelt is a single crystal grown along the [110] direction. Figure 3c shows the high-resolution TEM image taken from the Bi_2Te_3 nanobelt. The fringe spacing of 0.219 nm observed in this HRTEM image agrees well with the spacing between the (110) planes. This image further

confirms that the as-grown nanobelt is defect-free single crystal with high quality.

After Bi_2Te_3 nanobelts were fixed on the underlying Pt electrodes, it was found that the single nanobelt exhibits an extremely high resistance up to a few $\text{G}\Omega$, and that the obtained I – V curve is nonlinear. This may be ascribed to the thin oxide layer covering the nanobelts. Because of the existence of a thin oxide layer, the carriers flow through the oxide layer in a tunneling manner, which makes the nonlinear behavior of I – V curve. To avoid introducing deviation into electrical measurement, FIB techniques were employed to make the reliable electrical contacts between Bi_2Te_3 nanobelt and the Pt electrode. The process of making electrical contacts involves two steps: first, the thin oxide layer was removed by using Ga-ion beam sputtering technique when the image scanning of the sample was conducted; second, a few amount of Pt–hydrocarbon gas was injected on to the sample, and small rectangle Pt electrical contacts were formed by focusing the Ga-ion beam on the cross area between Bi_2Te_3 single crystal nanobelt and underlying Pt electrodes. A SEM image of

Fig. 3 **a** Low-magnification TEM image of a single Bi_2Te_3 nanobelt, **b** SAED pattern of the single Bi_2Te_3 nanobelt along the [001] zone axis, **c** high-resolution TEM image of the Bi_2Te_3 nanobelt



Bi_2Te_3 nanobelt with a width of 180 nm prepared utilizing this technique is shown in Fig. 4a. Two small rectangles in deep color at the ends of this nanobelt are the deposited Pt electrical contacts. After the electrical contacts were formed, the resistance of Bi_2Te_3 single crystal nanobelt decreased to 47 k Ω at 283 K, and the estimated resistivity is about $4.22 \times 10^{-3} \text{ } \Omega\text{cm}$.

Figure 4b shows the I - V curves of Bi_2Te_3 single crystal nanobelt measured in the temperature region from 233 to 383 K. The I - V curve is linear, indicating that the electrical contacts between Bi_2Te_3 nanobelt and electrodes are ohmic. The I - V curves maintain linear behavior well with the variations of temperature, indicating that the electrical contacts as prepared are thermally stable. The conductivity of the Bi_2Te_3 single crystal nanobelt was calculated as $0.47 \times 10^3 \text{ } \Omega^{-1} \text{ cm}^{-1}$ at room temperature, which is a little lower than that of bulk material ($\sigma_{\text{bulk}} = 0.9 \times 10^3 \text{ } \Omega^{-1} \text{ cm}^{-1}$) [21] but notably higher than that of the thin film ($\sigma_{\text{film}} = 0.17 \times 10^3 \text{ } \Omega^{-1} \text{ cm}^{-1}$) [22] and the pressure injected nanowires ($\sigma_{\text{nanowire}} = 0.21 \times 10^3 \text{ } \Omega^{-1} \text{ cm}^{-1}$) [23]. The above experimental results mean that the Bi_2Te_3 nanobelts grown by using VLS process are single crystals with high quality.

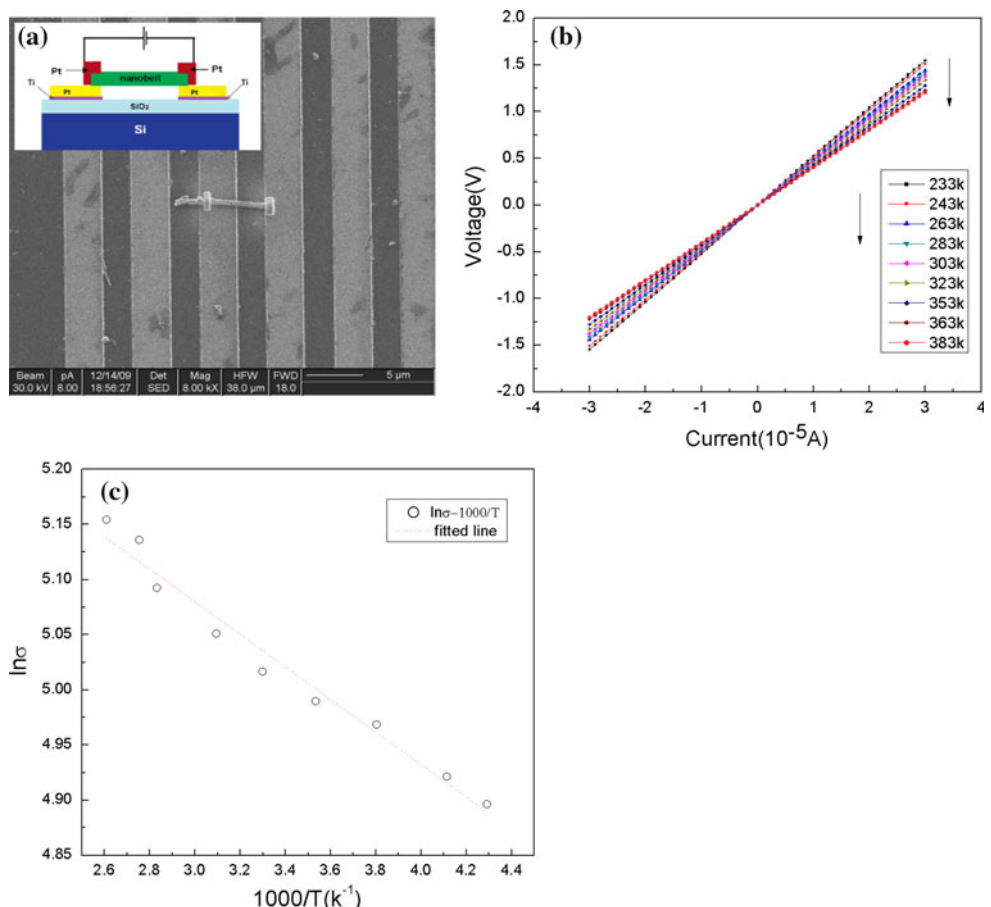
To investigate the transport properties of Bi_2Te_3 single crystal nanobelts, the temperature dependence of the conductivity was also measured. Figure 4c plots the conductivity of Bi_2Te_3 single crystal nanobelt as a function of the

inverse temperature. The conductivity increases with the increase of the temperature. This σ - T curve illustrates a semiconductor behavior of the as-grown Bi_2Te_3 nanobelts. The experimental data can be fitted by using the formula:

$$\sigma = \sigma_0 \exp\left(\frac{-\Delta E_a}{2KT}\right) \quad (1)$$

where ΔE_a is the activation energy, and K is the Boltzmann constant, σ is the conductivity. Bismuth telluride is an anisotropic material with a layered crystal structure. The conductivity parallel ($\sigma_{//}$) and perpendicular (σ_{\perp}) to the layers are different, and thus the corresponding activation energies ($\Delta E_{a//}$ and $\Delta E_{a\perp}$) are different [24–26]. As Bi_2Te_3 single crystal nanobelts as obtained grew along [110] direction, parallel to the layers, the activation energy acquired is the one parallel to layers. $\Delta E_{a//}$ was estimated as about 25 meV from the slope of the fitted line as shown in Fig. 4c, a little smaller than that as reported (36 meV) [27]. The activation energy is much smaller than the band gap of Bi_2Te_3 (150 meV), indicating that the carriers are excited from the impurity level, rather than from the valence band, in this temperature region [27]. This result suggests that the thermal activation of carriers is the dominant transport mechanism for Bi_2Te_3 single crystal nanobelts. The similar transport mechanism has been observed for nanoneedle [28], nanotube [29] and nanobelt [30] devices.

Fig. 4 **a** SEM image of the fabricated Bi_2Te_3 single crystal nanobelt device, **b** $I-V$ curve of Bi_2Te_3 single crystal nanobelt measured from 233 to 383 K, **c** the temperature dependence of the conductivity for Bi_2Te_3 single crystal nanobelt



Conclusions

In summary, Bi_2Te_3 single crystalline nanobelts were successfully synthesized through a VLS process. The SAED pattern and HRTEM image identified that the as-grown Bi_2Te_3 nanobelts are single crystalline, and the growth axes is along the [110] direction. Bi_2Te_3 single crystal nanobelt shows a semiconductor behavior. It was also observed that the thermal activation of carrier dominated the transport mechanism. Bi_2Te_3 nanobelts grown by VLS have high conductivity, indicating a potential for the application of high efficiency thermoelectric devices.

Acknowledgement This work was financially supported by the state key program for basic research of China under the Grant No. 2007CB935401.

References

- Huang BL, Kaviani M (2008) Phys Rev B 77:125209
- Mishra SK, Satpathy S, Jepsen O (1997) J Phys Condens Matter 9:461
- Zhang HJ, Liu CX, Qi XL, Dai X, Fang Z, Zhang SC (2009) Nat Phys 5:439
- Moore JE, Balents L (2007) Phys Rev B75:121306
- Kane CL, Mele EJ (2005) Phys Rev Lett 95:146802
- von Klitzing K, Dorda G, Pepper M (1980) Phys Rev Lett 45:494
- Tsui DC, Stormer HL, Gossard AC (1982) Phys Rev Lett 48:1559
- Sheng DN, Weng ZY, Sheng L, Haldane FDM (2006) Phys Rev Lett 97:036808
- Zhou J, Jin CQ, Seol JH, Li XG, Li S (2005) Appl Phys Lett 87:133109
- Kim Y, Cho S, Di Venere A, Wong GKL, Ketterson JB (2001) Phys Rev B 63:155306
- Bos JWG, Zandbergen HW, Lee MH, Ong NP, Cava RJ (2007) Phys Rev B 75:195203
- Dresselhaus MS, Chen G, Tang MY, Yang RG, Lee H, Wang DZ, Ren ZF, Fleurial JP, Gogna P (2007) Adv Mater 19:1043
- Sales BC (2002) Science 295:1248
- Venkatasubramanian R, Siivola E, Colpitts T, O'Quinn B (2001) Nature 413:597
- Bottner H, Chen G, Venkatasubramanian R (2006) MRS Bull 31:211
- Prieto AL, Sander MS, Martin-Gonzalez M, Gronsky R, Sands T, Stacy AM (2001) J Am Chem Soc 123:7160
- Sander MS, Prieto AL, Gronsky R, Sands T, Stacy AM (2002) Adv Mater 14:665
- Sander MS, Gronsky R, Sands T, Stacy AM (2003) Chem Mater 15:335
- Zhao XB, Ji XH, Zhang YH, Zhu TJ, Tu JP, Zhang XB (2005) Appl Phys Lett 6:86
- Xiao F, Yoo B, Lee KH, Myung NV (2007) J Am Chem Soc 129:10068
- Rowe D (2006) Thermoelectrics handbook: macro to nano. Taylor & Francis, New York

22. Das V, Soundararajan N (1988) Phys Rev B37:4552
23. Jones P (2006) Int Conf Thermoelectr 69:3
24. Nassary MM, Shaban HT, El-Sadek MS (2009) Mater Chem Phys 113:385
25. Bejenari I, Kantser V (2008) Phys Rev B 78:115322
26. Huang BL, Kaviany M (2008) Phys Rev B 77:125209
27. Nassary MM, Shaban HT, El-Sadek MS (2009) Mater Chem Phys 113:385
28. Liu X, Li C, Han S, Han J, Zhou C (2003) Appl Phys Lett 82:1950
29. Zhou C, Kong J, Dai H (2000) Appl Phys Lett 76:1597
30. Shen GZ, Chen PC, Bando Y, Golberg D, Zhou CW (2008) Chem Mater 20:7323